Space Weather®

Key Points:

- A 4D-Var-based new global ionosphere electron density assimilation model Neustrelitz Electron Density Assimilation Model (NEDAM) is presented
- The background covariance matrix is approximated by a Gaussian-Markov random field and the observation covariance is improved
- The accuracy of NEDAM is evaluated using simulated Global Navigation Satellite System observations and two ionosondes and COSMIC-1 data

Supporting Information:

Supporting Information may be found in the online version of this article.

Correspondence to:

L. Yuan,
liangliang.yuan@dlr.de

Author Contributions:

Conceptualization: L. Yuan
Data curation: L. Yuan
Formal analysis: L. Yuan
Funding acquisition: M. M. Hoque
Investigation: L. Yuan
Methodology: L. Yuan
Project Administration: M. M. Hoque
Software: L. Yuan
Validation: L. Yuan, Timothy Kodikara
Visualization: L. Yuan
Writing – original draft: L. Yuan
Writing – review & editing: M. M. Hoque, Timothy Kodikara

The Four-Dimensional Variational Neustrelitz Electron Density Assimilation Model: NEDAM

L. Yuan[1] , M. M. Hoque[1], and Timothy Kodikara[1]

[1]German Aerospace Center (DLR), Institute for Solar-Terrestrial Physics, Neustrelitz, Germany

Abstract With the development of the Global Navigation Satellite System (GNSS) and regional augmentation systems, the influence of the ionosphere on GNSS signals is becoming increasingly important. It is also of particular interest to retrieve the electron density distribution from GNSS observations. We have successfully developed a four-dimensional variational assimilation scheme, the Neustrelitz Electron Density Assimilation Model (NEDAM), and verified NEDAM by a simulation study using a European ground-based GNSS network. The performance of NEDAM is validated using two ionosondes and COSMIC-1 radio occultation observations during the September 2017 geomagnetic storm period. The critical frequency of the F2 layer in NEDAM is much more accurate than that of a physics-based model driven by observed geophysical indices or the Neustrelitz Electron Density Model (NEDM), when compared to data from two ionosondes. During the storm, the root mean square error of the F2-layer critical frequency with respect to the two ionosondes is improved by 0.54 and 0.42 MHz, respectively. We also compare two co-located electron density profiles from the COSMIC-1 mission with NEDAM and NEDM. It is found that NEDAM is able to reconstruct well not only the peak density but also the peak density height, which is missing in the previous research.

Plain Language Summary With the development of ground- and space-based observation techniques of the upper atmosphere, the capability of monitoring the variation of the Earth's ionosphere is increased drastically. However, due to the lack of three-dimensional observations with a good coverage, reliable and well defined scheme is required for extracting three-dimensional snapshots of the Earth's ionospheric electron density. This work presents an advanced four-dimensional variational scheme NEDAM in the region of 60–20,000 km above the Earth's surface. The work also validates the tomography results with multiple ionospheric observations from satellites and ground-based radar instruments and compares with empirical and physical models. It is usually a challenge for assimilative models to reproduce the ionospheric parameters such as the peak density height accurately during geomagnetic storms. The performance of NEDAM is validated against two ionosondes and COSMIC radio occultation observations during the September 2017 geomagnetic storm period. The critical frequency of F2-layer in NEDAM is much more accurate than that of NEDM with respect to the two ionosondes in the region of interests. The developed method will be applied in near real-time to space weather monitoring, GPS positioning and navigation, as well as to improve our understanding of the morphology and dynamics of the ionosphere.

1. Introduction

It is of particular interest to retrieve the electron density distribution from Global Navigation Satellite System (GNSS) observations due to its high density and broad spatial-temporal coverage. There are several commonly used methods such as Computerized Ionospheric Tomography (CIT), Bayesian analysis and Kalman filter (Bust et al., 2001; Prol et al., 2021; Scherliess et al., 2004). However, different methods differ in many aspects including computational cost, data storage and management cost, compatibility for different kinds of observations and flexibility in practical applications.

Several different techniques are developed to perform posterior analyses of the ionospheric electron density. One of the traditional techniques is CIT. CIT is a direct inversion technique that develops a two-dimensional electron density specification from a series of one-dimensional ionospheric observations and various minimization criteria (Kronschnabl et al., 1997; Raymund, 1995; Raymund et al., 1994). Similar work by other groups have led to the development of more advanced spatial analysis techniques. Howe et al. (1998) developed a Kalman filter method for ionospheric reconstruction based on spherical harmonics and Empirical Orthogonal Function describing the horizontal and vertical distribution, respectively. Manuel Hernández-Pajares☐ et al. (1999, 2002)

developed a voxel-based Kalman filter of the vertical electron content using GNSS-TEC measurements from ground receivers and radio occultation receivers and ionosondes. Schunk et al. (2004) described a Global Assimilation of Ionospheric Measurements tool. They have implemented a Gauss-Markov Kalman filter and a full physics-based Kalman filter is under development. Bust et al. (2004) introduced IDA3D based on 4D-Var in data space. Different kinds of measurements such as GNSS total electron content (TEC), vertical sounding from ionosonde, radio occultation and in situ measurements can be assimilated in IDA3D (Bust & Immel, 2020). A four-dimensional variational data assimilation technique was used to more accurately estimate the South African regional ionosphere and to reconstruct three-dimensional images of the ionospheric hole created during Kwangmyongsong-4 rocket launch (Ssessanga et al., 2018, 2019).

In all the literature mentioned above, ionospheric observations are considered as independent observations, that is, there is no correlation between the noise of two different observations. However, this is not the case if we consider two consecutive signals that are close to each other or have the same transmitter and receiver. Considering this, we are motivated to take the observation geometry into account when constructing the observation covariance matrix. In addition, the horizontal correlation length is determined in a mathematically rigorous manner by maximum likelihood estimation (MLE). The success of data assimilation strongly depends on the accuracy of the background model and a good estimation of the background model covariances, indicating that the assimilation results differ when different background models are used. In this study, we present for the first time a real-time electron density assimilation combining different types of observations with the newly developed climatological electron density model, the Neustrelitz Electron Density Model (NEDM). A good electron density assimilation should not only converge uniformly to the observations, but also resolve the horizontal and vertical distributions of the electron densities. The accuracy of the electron density assimilation is evaluated in several aspects, including all important physical quantities such as the TEC, the critical frequency of the F2 layer (foF2), and the corresponding peak height (hmF2). We also compare our results with the current capabilities of a well-established physics-based model, the thermosphere-ionosphere-electrodynamics general circulation model (TIEGCM; Richmond et al., 1992).

The paper is organized as follows. Section 2 introduces four-dimensional variational data assimilation (4D-Var) and the numerical method upon which NEDAM is developed. Section 3 contains general descriptions of simulations and real GNSS data used in this study. In Section 4 we present the main initial results and discussions of NEDAM in both simulation and real data cases. In Section 5, we conclude the current status of NEDAM development as well as the future improvements.

2. The NEDAM Approach Using 4D-Var Assimilation

2.1. Background Electron Density Model: NEDM

The ionospheric plasma density shows both the long-term (climatology) and short-term (weather) variations. The background electron density model may contain the climatological variation of the ionosphere while the assimilation refines the background model with the short-term variations. The 3D electron density model NEDM presented here is established by superposing electron density models of the plasmasphere and the ionosphere consisting of separate F and E-layer distributions of electron density. This model describes the spatial and temporal variability of the above-mentioned ionospheric key parameters as a function of local time, geographic or geomagnetic location, solar irradiation, and solar activity. Hoque et al. (2022) presented a comprehensive validation of NEDM using in-situ data from DMSP (Defense Meteorological Satellite Program), Swarm, Van Allen Probes and ICON (Ionospheric Connection Explorer) missions, topside TEC data from COSMIC/FORMOSAT-3 mission, bottom side TEC data from TOPEX/Poseidon mission, and ground-based TEC data from International GNSS Service covering both high and low solar activity conditions. A background ionosphere electron density model is essential in data assimilations to provide apriori information and fill data gaps in areas where there are no data. The accuracy of the background model in a climatological sense is one of the most important factors that affect the success of data assimilation since the background covariance information is highly dependent on the background model. In order to achieve a complete coverage from ground to GPS satellites the background ionosphere model will also need to include a plasmasphere model, since plasmaspheric electron content may contribute more than 60% of the total TEC in the line-of-sight direction especially during the local night. The NEDM has the heritage of being a member of a family of ionospheric models developed at the German Aerospace Center (DLR) in Neustrelitz over the last 20 years. These include global empirical models for the ionospheric TEC, F2-layer peak

density NmF2, and peak density height hmF2, which are used in operational space weather services. The NEDM is composed of the following domain-specific models: Neustrelitz TEC Model (Jakowski et al., 2011), Neustrelitz Peak Density Model (Hoque & Jakowski, 2011), Neustrelitz Peak Height Model (Hoque & Jakowski, 2012), and Neustrelitz Plasmasphere Model (NPSM; Jakowski & Hoque, 2018). The NPSM describes electron density distribution in the topside ionosphere and plasmasphere by addressing not only McIlwain L-shell dependencies of the electron densiy but also by considering altitude dependencies describing the coupling between the ionosphere and plasmasphere. Although the number of model coefficients and parameters is rather small, these sub models describe the main ionospheric/plasmaspheric features with good quality. Three dimensional NEDM is composed of global models NTCM, NPDM NPHM and NPSM describing ionosphere key parameters, such as TEC, NmF2 hmF2 and plasmaspheric distribution. Each sub-model is driven by the solar radio flux index F10.7 and the 3D global outputs are realized by combining multiple Chapman layers with a superposed exponential decay function describing the plasmasphere (i.e., NPSM).

2.2. Observation Equation

In order to estimate a set of unknown electron density values based on the GNSS TEC measurements, the GNSS TEC is represented by a discrete integral of electron densities along the line of sight direction. The equation to solve for the unknown electron density x in each voxel

$$d = Tx + \varepsilon \tag{1}$$

where d is the GNSS TEC measurement vector, T is the design matrix associated with the assigned voxels, and ε is the system and measurement noises. The linear interpolation is adopted for the four nearest voxels to the intersection point with the weight of inverse of the distance between the intersection point and voxels.

2.3. Background Precision Matrix

The main idea is to approximate the Matérn correlation function (Lindgren et al., 2011) by a Gaussian Field satisfying a group of stochastic partial differential equation (SPDE). The Matérn correlation function between two locations u and $v \in \mathbb{R}^d$ is defined as

$$C(u, v) = \frac{1}{2^{v-1}\Gamma(v)} (\kappa \|u - v\|)^v K_v(\kappa \|u - v\|) \tag{2}$$

where v is the smoothness parameter, κ is the range parameter, K_v is the modified Bessel function of the second kind, Γ is the gamma function. A Gaussian Field $x(u)$ with the Matérn covariance is a solution to the linear fractional SPDE (Lindgren et al., 2011)

$$\left(\kappa^2 - \Delta\right)^{\frac{\alpha}{2}} x(u) = W(u) \tag{3}$$

where $\alpha = v + d/2$. For example, with $v = 1/2$, $d = 3$, $\kappa = 1$ and the asymptotic form of modified Bessel function of second kind

$$K_v(z) = \sqrt{\frac{\pi}{2}} \frac{e^{-z}}{\sqrt{z}} \left(1 + O\left(\frac{1}{z}\right)\right) \quad \text{when } |z| \to \infty, \tag{4}$$

the Matérn correlation function could be approximately expressed as

$$C(u, v) = \exp(-(\|u - v\|)) + \sqrt{\frac{\pi}{2}} \frac{e^{-\|u - v\|}}{\sqrt{\|u - v\|}} O\left(\frac{1}{\|u - v\|}\right), \tag{5}$$

where we use the fact $\Gamma(1/2) = \sqrt{\pi}$ and the definition of the Euclidean norm

$$\|u - v\| = \sqrt{\left(\frac{u_x - v_x}{l_x}\right)^2 + \left(\frac{u_y - v_y}{l_y}\right)^2 + \left(\frac{u_z - v_z}{l_z}\right)^2}, \tag{6}$$

where u_x, u_y and u_z are x, y, and z coordinates of u, v_x, v_y and v_z are x, y, and z coordinates of v, l_x, l_y and l_z are correlation lengths in x, y, and z directions, respectively. to approximate the precision matrix of an exponential

correlation function by the pseudo-partial differential operator $L = \left((1/2)^2 - \Delta\right)^1$. Following Norberg et al. (2018) and Roininen et al. (2018), the truncated spectrum method for Gaussian correlation function with finite differencing is implemented as follows:

$$L_0 = \sqrt{\frac{c_0}{\sigma} s_{\text{lat}} s_{\text{lon}} s_{\text{alt}}} \circ I_{n\text{lat}} \otimes I_{n\text{lon}} \otimes I_{n\text{alt}} \tag{7}$$

$$\begin{cases} s_{\text{lat}} = g_{\text{lat}}/l_{\text{lat}} \\ s_{\text{lon}} = g_{\text{lon}}/l_{\text{lon}} \\ s_{\text{alt}} = g_{\text{alt}}/l_{\text{alt}} \end{cases} \tag{8}$$

$$\begin{cases} L_{1\text{lat}} = \dfrac{\sqrt{\frac{c_1}{\alpha} s_{\text{lat}} s_{\text{lon}} s_{\text{alt}}} \circ L_{n\text{lat}} \otimes I_{n\text{lon}} \otimes I_{n\text{alt}}}{s_{\text{lat}}} \\[2em] L_{1\text{lon}} = \dfrac{\sqrt{\frac{c_1}{\alpha} s_{\text{lat}} s_{\text{lon}} s_{\text{alt}}} \circ I_{n\text{lat}} \otimes L_{n\text{lon}} \otimes I_{n\text{alt}}}{s_{\text{lon}}} \\[2em] L_{1\text{alt}} = \dfrac{\sqrt{\frac{c_1}{\alpha} s_{\text{lat}} s_{\text{lon}} s_{\text{alt}}} \circ I_{n\text{lat}} \otimes I_{n\text{lon}} \otimes L_{n\text{alt}}}{s_{\text{alt}}} \end{cases} \tag{9}$$

$$L_2 = \frac{\sqrt{\frac{c_2}{\alpha} s_{\text{lat}} s_{\text{lon}} s_{\text{alt}}} \circ I_{n\text{lat}} \otimes I_{n\text{lon}} \otimes \left(L_{n\text{alt}}^T L_{n\text{alt}}\right)}{s_{\text{alt}}^2} + \frac{\sqrt{\frac{c_2}{\alpha} s_{\text{lat}} s_{\text{lon}} s_{\text{alt}}} \circ I_{n\text{lat}} \otimes I_{n\text{alt}} \otimes \left(L_{n\text{lon}}^T L_{n\text{lon}}\right)}{s_{\text{lon}}^2}$$
$$+ \frac{\sqrt{\frac{c_2}{\alpha} s_{\text{lat}} s_{\text{lon}} s_{\text{alt}}} \circ I_{n\text{lat}} \otimes I_{n\text{lon}} \otimes \left(L_{n\text{lat}}^T L_{n\text{lat}}\right)}{s_{\text{lat}}^2} \tag{10}$$

$$L = \begin{pmatrix} L_0 \\ L_{1\text{lat}} \\ L_{1\text{lon}} \\ L_{1\text{alt}} \\ L_2 \end{pmatrix} \tag{11}$$

$$\text{P} = L^T L \tag{12}$$

where I_n represent identity matrices with dimension n, L_1 represent the first-order difference matrix, L_2 represents the second-order difference matrix and σ represents the variance masks generated by the background model. Note that the variance mask is assumed to be 0.4 times the background electron density (Yue et al., 2007). The symbol "$\circ$" is the Hadamard product and the symbol "$\otimes$" is the Kronecker product. The specific form of a correlation function depends on c_k. In this study, the parameter c_k is chosen as the same value in Norberg et al. (2018) for the squared exponential correlation function. However, in the paper by Norberg et al. (2018), they adopted the squared exponential function as the correlation function in spherical coordinates without any correction of the latitude effect. Since the correlation function is defined on the uniform grid in zonal direction, it may happen that in the high latitude region the great circle distance between two voxels with higher latitude and some fixed longitudinal difference will decrease drastically compared to those in the lower latitude region. And therefore, a nonuniform correlation length is needed in the longitude directions. Considering this, we take the latitude effect into consideration through a re-scaling of grids in the finite difference method since for global data assimilation the latitude effect can be large in the polar regions. The correlation length in zonal direction varies with latitudes as follows

$$\text{corr\_len(lat)} = \text{corr\_len(0)} / \cos(\text{lat}) \tag{14}$$

where corr_len(0) is the longitudinal correlation length at the equator. Due to the singularity of cosine function at poles, the correlation length is assumed to be constant at hight latitude region, that is, 6090° latitude. In this case, the s_{lon} is necessarily a vector rather than a scalar. We also note that the correlation length may influence the magnitude of approximated covariances since L_0, L_1, and L_2 are proportional to $l^{3/2}$, $l^{1/2}$, and $l^{-1/2}$, respectively.

2.4. Observation Covariance

In previous studies, different measurements are considered as independent measurements in ionospheric data assimilations and therefore, the observation covariance matrix is defined as a diagonal matrix. However, the intersections among different measurements must result in correlations between one and the other measurements. Taking the signal geometry into consideration, we calculated the covariance of the integrated random variables slant TEC (STEC) as follows

$$\text{Cov}\left(\text{STEC}_{s_i}, \text{STEC}_{s_j}\right) = \iint\limits_{s_i s_j} \text{Cov}\left(\text{Ne}(s_i)\text{Ne}(s_j)\right) dx_i dx_j + \text{Cov}\left(b_{s_i}, b_{s_j}\right) \tag{15a}$$

$$\text{Cov}\left(b_{s_i}, b_{s_j}\right) = \text{Cov}\left(\text{dcb}_i^{\text{sat}}, \text{dcb}_j^{\text{sat}}\right) + \text{Cov}\left(\text{dcb}_i^{\text{rcv}}, \text{dcb}_j^{\text{rcv}}\right) \tag{15b}$$

where $\text{Cov}(\text{STEC}_i, \text{STEC}_j)$ is the covariance between the two observations STEC_i and STEC_j, $\text{Ne}(x_i)$ is the electron density at point x_i along the ith signal path s_i, $\text{dcb}_i^{\text{rcv}}$ is the receiver DCB of the ith signal, $\text{dcb}_i^{\text{sat}}$ is the satellite DCB of the ith signal and s_i is the ith signal path along the line of sight. A proof of the above formula is given in Appendix A.1. The first term on the right-hand side of Equation 15a represents the ionospheric modeling errors in the TEC calibration procedure while the second term represent the covariance from the receiver and satellite differential code biases. Simply speaking, the observation covariance is not only composed of the bias but also the imperfectness of the ionospheric modeling used in the TEC calibration procedure. No matter whether the signal is transmitted (or received) by the same transmiiter (or receiver) or not, two signals of similar geometries ought to be correlated with each other via the same ionosphere modeling process in the calibration procedure. In this case, we assume the last term of above Equation 15a is zero for two independent satellite-receiver links. This observation covariance abandoned the independent assumption that is commonly used, which is more appropriate especially for the intersected observations during disturbed period. The introduction of this assumption helps mitigating the overestimation or underestimation of electron density at the intersected gridpoints because of the introduction of non-zero off-diagonal terms. In this study, the satellite and receiver DCB errors are set to 0.1 and 1TECU, respectively (Yuan et al., 2020a, 2020b, 2021a). And for simplicity, the first term of the right hand side of Equation 15a is assumed to be 0, which assumes a perfect VTEC modeling in the TEC calibration procedure. The observation precision matrix can be represented by the inverse of the observation covariance matrix since the dimension of the observation covariance matrix which is typically several thousands is much less than that of background covariance matrix which is typically several millions in this study.

2.5. Space Tapering for Sparse Background Covariance Matrix

Considering the introduction of off-diagonal terms in the observation covariance, the first term in the right hand side of Equation 15a can be approximated by a space tapering of Gaussian covariance.

$$C(u, v) = \alpha(u, v)\exp\left(-\frac{1}{2}\left[\left(\frac{u_x - v_x}{l_x}\right)^2 + \left(\frac{u_y - v_y}{l_y}\right)^2 + \left(\frac{u_z - v_z}{l_z}\right)^2\right]\right) \tag{16}$$

$$\alpha(u, v) = \sigma_u \cdot \sigma_v \tag{17}$$

where σ_u and σ_v is the standard deviation at u and v. For two voxels u, v satisfying $u_x - v_x > c$ where c is a correlation mask, or the similar condition in the other two coordinate directions, the a priori correlation function is approximated by 0. Note that in this section, Gaussian correlation function in Equation 16 is approximated in covariance matirx rather than in precision matrix in Section 2.2. According to the well-known paper by Gaspari and Cohn (1999), we adopt the compactly supported fifth-order piecewise function as an space tapering function for Gaussian correlation function. Note that the correlation distance l_x serves as a spatially smoothing factor. The validity of the Gaussian function to a correlation function is shown in Appendix A.2.

2.6. Optimal Parameter Determination in the Gaussian Correlation Function

A MLE procedure is adopted for determining the optimal parameter set in the Gaussian correlation function. Taking into consideration the location-dependency of the correlation lengths, the MLE procedure is applied to three kinds of regions, namely high-, mid-, and low-latitude regions separately. Yue et al. (2007) and Shim et al. (2008) analyzed the correlation lengths on VTEC level and reported that the correlation lengths in latitude and longitude direction depend on the considered latitude domain. The different driving forces are mentioned as possible reasons. Consequently, on global scale the assumption of stationary correlation lengths in the correlation function may become invalid and the necessity of location-dependent correlation lengths arises. Lin et al. (2015) constructed a covariance model with location-dependent correlation lengths based on empirical orthogonal functions and their coefficients. It is shown that such a covariance model outperforms a stationary covariance model when both STEC and radio occultation measurements are assimilated.

We propose that the covariance parameter vector $l = (l_1, l_2, l_3)$ can be obtained via an MLE. For that purpose, the electron density is assumed to be Gaussian distributed and hence line (or curve) integrals of electron densities. The multivariate Gaussian probability density function with STEC observations can be written as follows

$$f_l(\text{STEC}) = \frac{1}{\sqrt{(2\pi)^N \cdot |\Sigma_l|}} \exp^{-\frac{1}{2}(\text{STEC}-u)^T \Sigma_l^{-1}(\text{STEC}-u)} \tag{18}$$

where $f_l(\text{STEC})$ is the function needed to be maximized, N is the dimension of the space, Σ_l is the covariance matrix as a function of parameter vector l, STEC is the GNSS STEC measurement and u is the background STEC. Consequently, the MLE $\hat{l}$ of the parameter vector $l = (l_1, l_2, l_3)$ is

$$\hat{l} = \arg\max \ln f_l(\text{STEC}) = \arg\min \ln|\Sigma_l| + (\text{STEC} - u)^T \Sigma_l^{-1}(\text{STEC} - u) \tag{19}$$

However, the MLE procedure based on ground GNSS observations is not able to provide any information on the vertical correlation length. In this study according to the MLE analysis, the horizontal correlation lengths at the equator is set to 5.8 and 10.4° in latitude and longitude, respectively. The vertical correlation lengths can be taken as the value of local atmospheric scale heights for simplicity. During night, the vertical correlation might be weakened due to the low level of photonization. Alternatively, the vertical correlation length can be estimated by the correlation coefficient r of the time series of the model electron density values in 24 hr

$$r = \frac{\int_{t=0}^{t=24} \epsilon_x(t)\epsilon_y(t)dt}{\left|\int_{t=0}^{t=24} \epsilon_x(t)dt\right|\left|\int_{t=0}^{t=24} \epsilon_y(t)dt\right|} \tag{20}$$

$\epsilon_x(t)$ represents the error of electron density at height x and time t. According to Schwarz inequality, the vertical correlation r is a real number ranging from minus one to one. According to our correlation length analysis using ionosonde observations, a eighth-order polynomial regression is adopted for vertical correlation length modeling. The polynomial coefficients from highest to lowest order are 5.681e−38, −1.853e−31, 2.480e−25, −1.777e−19, 7.442e−14, −1.857e−08, 2.687e−03, −2.053e+02, and 6.378e+06. This polynomial is valid for ionosphere below 400 km and the correlation length is assumed to be continuous at 400 km and constant above 400 km.

2.7. Model Voxelization Strategy

In NEDAM, we use a regular numerical voxelization strategy in the horizontal dimension and an nonuniform strategy in the vertical dimension. The precomputed grid has a default spacing of 2.5° in latitude and 2.5° in longitude. For the default spacing described above, we get total 73×145 horizontal grid points. Considering typical ionospheric profile shape, it is reasonable to construct a denser voxelization in the typical E and F region and a sparser voxelization above the F region. We assume that the vertical grid consists of around 100 elements from 60 km up to 20,000 km. Vertical grid spacing is set to a high value of 10 km in the ionospheric E and F region since we are interested in the hmF2 variation which may be retrieved from data assimilations. Above F2-layer a geometric series is adopted considering slowly varying vertical structure.

$$h_n = h_0 + \frac{q^n - 1}{q - 1} \cdot dh \tag{21}$$

where h_n is the height of nth layer, q is a scaling factor which is 1.25 here, dh is set to 20 km.

Considering above mentioned spatial and vertical resolutions, the total number of grid points becomes a magnitude of 10^6 in the current NEDAM configuration.

2.8. Variational Problem

Following Courtier et al. (1994), the cost function in 4D-Var can be written as follows,

$$J(x(t_0)) = \frac{1}{2}[(x(t_0) - x_o^b(t_0))^T B_0^{-1}(x(t_0) - x_o^b(t_0)) + \sum_k (y_k - Hx(t_k))^T R_k^{-1}(y_k - Hx(t_k))] \tag{22}$$

where $x(t_0)$ represents the analysis state variable at time t_0, $x_o^b(t_0)$ the background state variable at time t_0, B_0^{-1} the background precision matrix, y_k the observation at time t_k, H the design matrix, R_k^{-1} the observation precision matrix and $x(t_k)$ the predicted state variable at time t_k. The state variable $x(t_0)$ to be analyzed could be estimated based on a minimization procedure of the cost function $J(x(t_0))$. It is commonly known to adopt the gradient descent or conjugate gradient method for minimizing the cost function. As long as the cost function is strictly convex and the projection from y_k to $x(t_k)$ is linear, every local minimum of $J(x(t_0))$ is a global minimum.

Since the background model in this study is fully empirical, we adopt a simple forecast model for 4D-Var depending on the relative motion between the ionosphere and solid Earth's rotation to the lowest order of approximation. The forecast model can be represented by a tranlsation along the zonal direction between the earth-fixed reference frame and inertia reference frame.

$$x(t_{k+1}) = R(t_{k+1} - t_k)x(t_k) \tag{23}$$

where R is the zonal translation matrix associated with time interval $\Delta t = t_{k+1} - t_k$. The rotation forecast model is assumed to be accuate and therefore there is no weak constraint term added on the right-hand side of the cost function.

2.9. Precondition of the Cost Function

In most cases, it is also beneficial to use incremental form of 4D-Var in the following preconditioning procedure (Courtier et al., 1994). Substituting $x(t_0) - x_o^b(t_0)$ with $U[x(t_0) - x_o^b(t_0)]$ and $U^T U = B_0^{-1}$, since B_0^{-1} is symmetric positive definite and define $v = U[x(t_0) - x_o^b(t_0)]$ so that $[x(t_0) - x_o^b(t_0)]^T B_0^{-1}[x(t_0) - x_o^b(t_0)] = v^T v$, it allows us to re-write the cost function as follows

$$J(v) = v^T v + (y' - HRU^{-1}v)^T R_k^{-1}(y' - HRU^{-1}v) \tag{24}$$

where $y' = y - HRx_o^b(t_0)$ and the subscript k is dropped for brevity. After solving this argument v minimizing the new cost function, the original state variable ψ^a can be retrieved by

$$x^a(t_0) = U^{-1}v + x_o^b(t_0) \tag{25}$$

It is also worth noting that the preconditioning procedure reduces the computational cost of the first term of the right-hand side of the cost function (22) from $O(n^2)$ to $O(n^1)$.

3. Data Source

3.1. Simulation

In the simulation study, the background electron density model NEDM is perturbed as the ionospheric truth. In order to initially evaluate the performance of the NEDAM, a 10% increment is added to perturbe the background model NEDM. Note that this perturbation does not influence the vertical structure or shape of the electron density profile as well as hmF2 value. About 50 GNSS ground stations near European region are selected for simulating

2017 251 220000
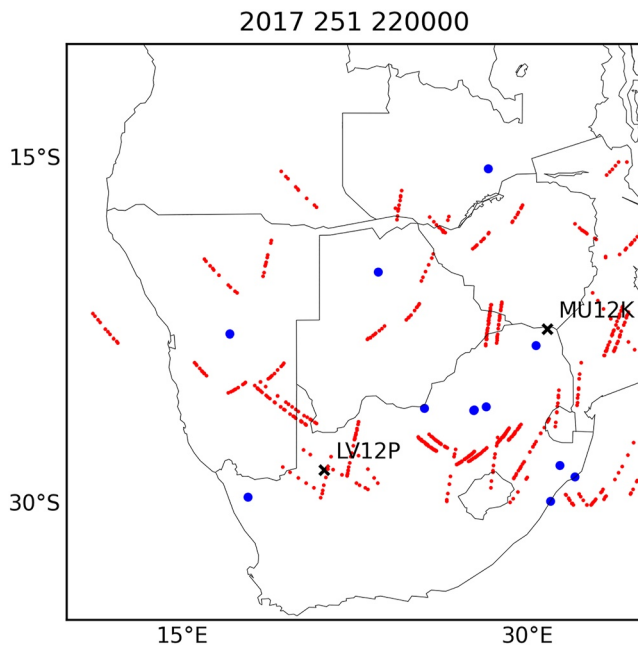
Figure 1. Geographical distributions of Global Navigation Satellite System (GNSS) stations (blue dots), ionosphere pierce points of the GNSS total electron content observations (red dots), and ionosonde stations MU12K and LV12P (black crosses) at 22:00 UT on 8 September 2017.

link geometries with 32 GPS satellites using the real GPS satellite orbits. The simulated observations are retrieved by line integrals of the electron densities produced by the perturbed electron density model on day of year 61 in 2011. The elevation mask for simulated data is set to 10° and the temporal sampling rate is set to 30 s.

3.2. Real Data

In this work, the data used for NEDAM are the post processed GNSS TEC provided by the MIT Haystack Observatory during Spetember 2017 geomagnetic storms, which are available at the CEDAR Madrigal database (http://cedar.openmadrigal.org/). For the period under investigation, the database provides GNSS measurements from around 20 stations over the African region, as presented in Figure 1 at 22:00 UT on 8 September 2017 while the daily distribution can be found in the Figure S1. The geomagnetic and interplanetary conditions were examined using the auroral electrojet index (AE), SYM-H index, three components of the Interplanetary Geomagnetic Field (IMF), solar wind plasma speed, proton temperature, and proton density measured at L1 lagrange point by DSCOVR satellite during 6–8 September 2017 in Figure 2. These data can be found at the NASA website https://spdf.gsfc.nasa.gov/. The first geomagnetic storm started with a Storm Sudden Commencement (SSC) started at 23:02 UT on 7 September 2017. The main phase started at 23:07 UT on 7 September and reaches the minimum SYM-H value of −146 nT at around 01:08 UT on 8 September. And the latter storm reached its maximum phase (SYM-H = −115 nT) at around 13:56 UT on 8 September. The IMF Bz showed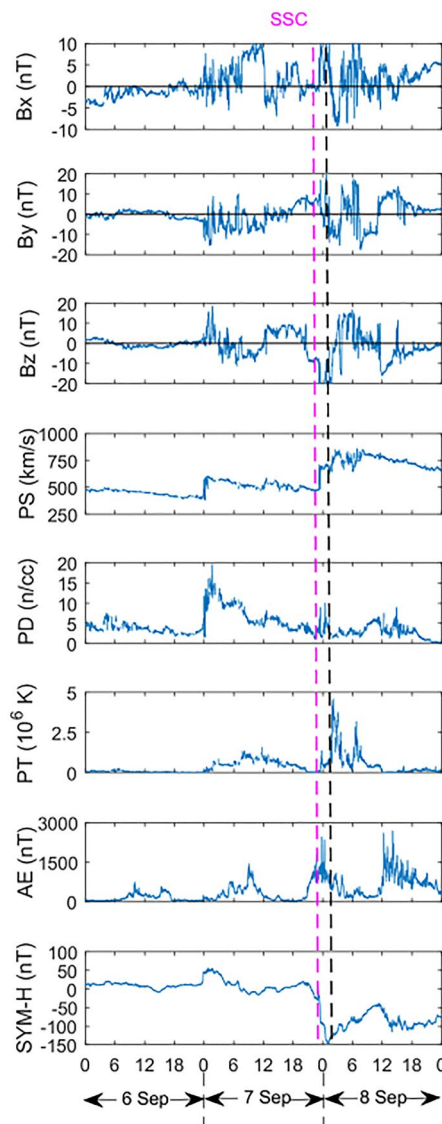 quite remarkable fluctuations on 7 and 8 September, which is supposed to be as a consequence of two SSC at 23:43 UT on 6 September and 23:02 UT on 7 September 2017. The first SSC caused the northward turning of IMF Bz around 0 UT on 7 September with a maximum value of approximately 18 nT. Subsequently, Bz kept southward for over 11 hr (from 01:00 to 12:00 UT) with an average value around −8 nT. It later had a sharp southward turn at approximately 20:40 UT and remained so until 23:30 UT on 7 September and attained its first minimum value of −20 nT at midnight. Then it reached the second minimum value of ∼−15 nT at 11:50 UT on 8 September. The AE index increased beyond 500 nT on 7 September between 03:00 and 10:00 UT. While the AE values as at the times of the first and second IMF Bz minima became suddenly enhanced and reached about 2300 and 2500 nT, respectively. The SYM-H index showed minima values of −146 and −115 nT at 01:08 UT and 13:56 UT on September 8, respectively.

4. Results and Discussion

4.1. Simulation Verification

Figure 3 shows the comparisons of altitude slices of electron density at constant longitude 15°E (see top panel) and at constant latitude 50°N at 12:00 UT on day of year 61 in 2011. We can see electron density enhancements in Figures 3b and 3e when comparing to Figures 3a and 3d. Figures 3c and 3f show that the electron density enhancements occur mainly in the mid-latitude region, which is consistent with the ground receiver distribution. It is worth noting that there is some small depletion near the equator in Figure 3c. This might be the result of the existence of horizontal gradients in the equatorial region. Figure 4a shows the differences between the background model and ionospheric truth and Figure 4b shows the differences between assimilation and ionospheric truth over European region. It can be seen over the region where the receiver distribution is quite dense the VTEC difference is significantly decreased. Esepecially in the mid-latitude region, the VTEC differences over three stations in Table 1 are decreased by 1 TECU, which shows that the assimilation process works well with a linear perturbation for VTECs and also shows a good capability of reconstructing the horizontal structures of the ionospheric electron density. Moreover, the VTEC error in 4D-Var assimilation at geographic location (38.51°N, −28.62°E) is much larger than that at location (52.32, 13.25). This is because the observations around the location (38.51°N, −28.62°E) is much coarser than those around the point (52.32°N, 13.25°E). It is known that the improvement of VTEC with respect to the truth shows a dependence on the observation geome-

Figure 2. Space weather indices during 6–8 September 2017. The purple dashed line represents the Storm Sudden Commencement at 23:02 UT on 7 September 2017. The black dashed line represents the sudden increase of solar wind plasma temperature and speed.
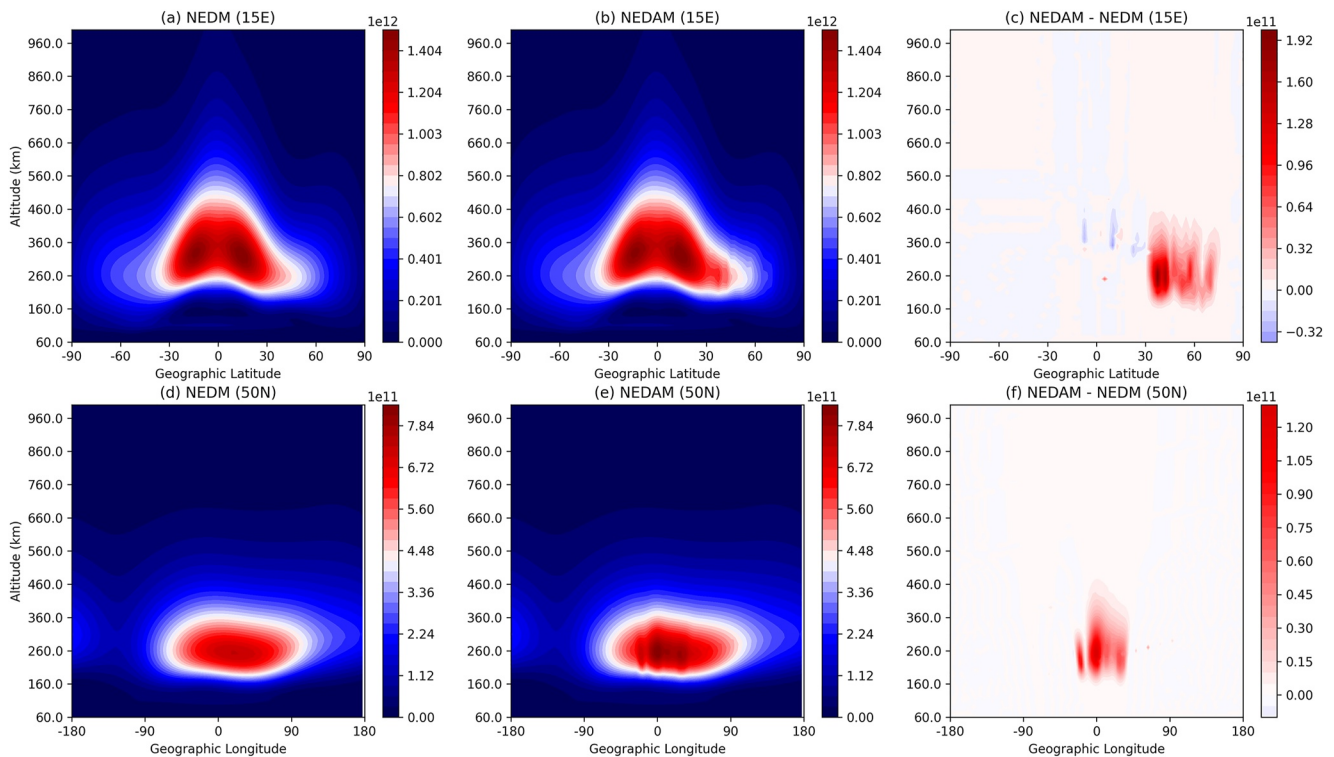
try, which means that the elevation and azimuth angles of the GNSS STEC observations determine the location where the VTEC improvement may occur. In order to evaluate the performance in the vertical structure reconstruction, Figure 5 shows the comparison of electron density profiles among background model, assimilation and ionospherci truth. As it is mentioned earlier, we mainly focus on the change of NmF2 rather than hmF2 since the vertical structure of the electron density is not changed. Figure 5 shows that the electron density profiles look similar in different locations. For example, the NmF2 values in assimilations are slightly lower than the truth except Figure 5a. In panel 5a, we can see that the topside electron densities are over-estimated with respect to the truth. This discrepancy could be due to insufficiency of observations and the improper constructions of vertical correlation lengths. Both of these two reasons can lead to an imperfect electron density profiles with repsect to a linear perturbation. In panels c and d, there is no significant change in the topside electron densities which should attribute the difference of the observation geometry. Results indicate that although the horizontal structure of the electron density is reconstructed quite well, the vertical structure is more variable and more difficult to recover.

### 4.2. Bottomside Ionosphere Validation Against Ionosonde Data

Figure 6 shows the horizontal slices of electron densities at 100, 200, 300, and 400 km from NEDM (see a, d), NEDAM (b, e), at mid-noon (13:00 UT) and pre mid-night (22:00 UT), respectively. The reason why these two specific time are chosen is to make the electron density maps in Figure 6 consistent in time with later discussions in Section 4.3. Figures 6c and 6f show the difference of electron densities between NEDM and NEDAM. During noon time, large electron density enhancements up to 10^{12}el/m^3 at peak density height are found while sporadic and small depletions may also occur. During nighttime, on the contrary, the values of electron densities of NEDAM in all layers are much smaller than those of NEDM.

To evaluate the performance of NEDAM during storm events, we compare the ionospheric electron densities with two ionosondes, MU12K ($-22.37°$N, $30.02°$E) and LV12P ($-28.5°$N, $21.2°$E). The ionosonde data are auto-scaled and obtained from the Global Ionosphere Radio Observatory (GIRO) at https://giro.uml.edu/didbase/. Figure 7 shows the time series images of the electron density profiles recorded at the two ionosonde stations with the sampling rate of 15 min on 8 September 2017. Strong enhancements can be seen starting at 06:00 UT for both ionosonde stations. However, for the LV12P ionosonde, the value of NmF2 is overestimated by NEDAM during

the enhancement, which could be caused by the lack of observations, the inclusion of low-elevation observations, and larger differential code bias errors induced by ionospheric variation during storm time. For the MU12K ionosonde, NmF2 values are better reconstructed in NEDAM due to better observational geometry. Figure 8 shows the comparison of critical frequency of F2 layer (foF2) between the MU12K and LV12P ionosondes, NEDAM, NEDM, and TIEGCM. Since NEDM is a data-based climatology, the comparison with TIEGCM provides a reference to the current capabilities of a well-established physics-based model driven by observed geophysical indices. In this study, we use the TIEGCM version 2.0 in the following configuration: latitude and longitude resolution is 2.5°, vertical scale-height is 0.25, the solar irradiance input is specified through the daily $F_{10.7}$ index and its running 81-day centered mean, the high latitude electric potential by the Heelis et al. (1982) ion convection model, and the lower atmospheric tidal forcing by the Hagan et al. (2001) global scale wave model. We also use the diurnal eddy diffusion coefficient from Qian et al. (2009) to add perturbations to the advective and diffusive transport. Here, the model estimated foF2 is linearly interpolated to the data location.

Figure 3. Comparisons of altitude slices of electron density at constant longitude 15°E and at constant latitude 50°N at 12:00 UT on day of year 61 in 2011.

The NEDM is unable to reproduce the ionospheric response to the 8 September 2017 space weather event. In general, the TIEGCM underestimates the critical frequency. For the MU12K case, the maximum foF2 in the TIEGCM is at about 12 UT. However, the maximum foF2 occurs about 4 hr earlier in the ionosonde measurements. For the LV12P case, TIEGCM shows a minor enhancement around 12 UT, but does not reproduce the
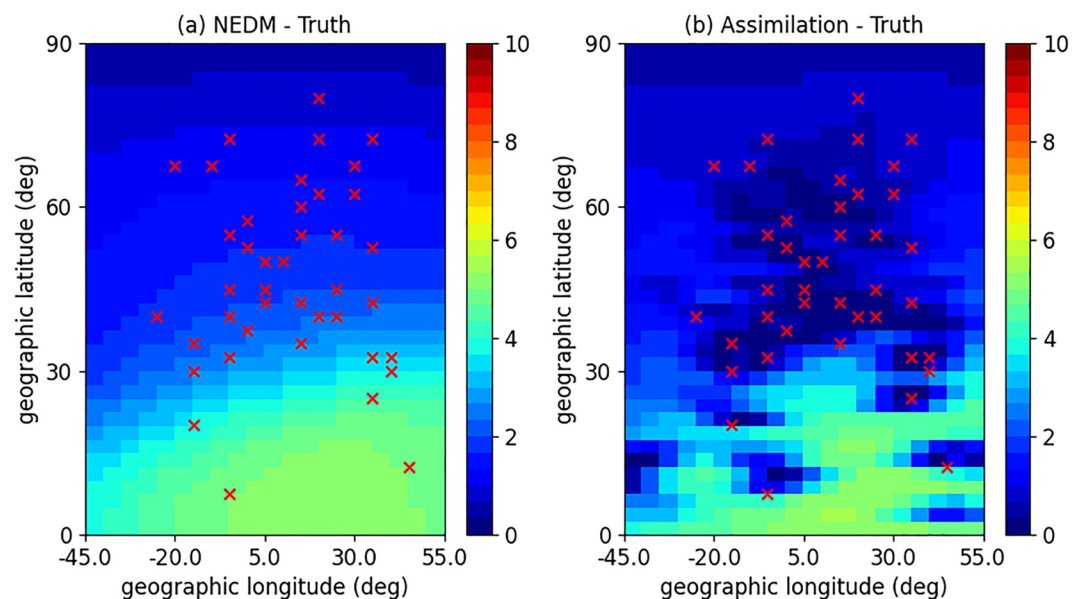
Figure 4. Comparison of VTEC differences between perturbed ionospheric truth generated by 10% increments of the background model and (a) Neustrelitz Electron Density Model, and (b) assimilation results at 12:00 UT on day of year 61 in 2011. The red crosses represent the simulated ground receivers. (Unit: TECU, 1TECU = 10^{16} el/m²).

Table 1
*VTEC Error at Four Selected Stations at 12:00 UT on Day of Year 61 in 2011*

Station location (lat, lon) [degrees]	VTEC error [TECU] (background)	VTEC error [TECU] (4D-Var assimilation)
(52.32, 13.25)	1.59	0.32
(51.85, −8.5)	1.54	0.66
(50.34, 30.89)	1.66	0.59
(38.51, −28.62)	1.71	0.81

magnitudes seen in the ionosonde data. The root mean square errors (RMSE) of TIEGCM with repsect to the ionosonde MU12K and LV12P are 2.20 and 2.38 MHz, respectively. In other words, TIEGCM captures certain diurnal characteristics of the observed foF2 but shows a clear systematic bias.

In terms of improvement of foF2 in NEDAM compared to NEDM, the RMSEs of daily foF2 decrease from 1.56 to 1.02 MHz for MU12K and from 1.57 to 1.15 MHz for LV12P. Besides the RMSE improvement, the overall trend is also improved in NEDAM. The Pearson correlation coefficients of foF2 increase from 0.72 to 0.92 for MU12K and from 0.77 to 0.93 for LV12P despite the rather sparse and non-uniform distribution of GNSS receivers.

4.3. Topside Ionosphere Validation Against Radio Occultation Data

Figure 9 shows the comparisons of electron density profiles between NEDAM, NEDM and COSMIC-1 radio occultation. Since COSMIC-1 mission was at the end of its lifetime, only one or two satellites provided good radio occultation observations during this geomagnetic storm. Fortunately, there are two radio occultation events which are co-located. The electron density profiles from NEDAM and NEDM are interpolated to the tangent points. In Figure 9a, the first radio occultation event started at around 13:12 UT at 26.46°S, 27.07°E and the electron density profile shows a typical daytime vertical structure with one density peak at F2-layer. The general structures in these three cases are similar. But we see that the heights of F2 peak among these three profiles are almost the same while the peak densities differ. The peak density in NEDAM is slightly lower than that in NEDM, which is consistent with the COSMIC radio occultation profile though the peak density in NEDAM is slightly under-estimated. In Figure 9b, the second radio occultation event started around 22:11 UT at 22.97°S, 33.52°E and the second electron density profile is quite different from the first one. The radio occultation technique may become less accurate due to the break of local spherical symmetry during storm time. This maybe one of the reasons for the occurrence of negative electron densities below F-layer peak in Figure 9b. The single peak structure is not present in the night-time event and the overall structure is more complicated. It can be seen that peak density in NEDM is over-estimated by 2.5 times of the peak density in COSMIC profile. In addition, the peak density height is also quite different, which is around 300 km in NEDM and 350 km in COSMIC. In NEDAM, a dual-peak structure
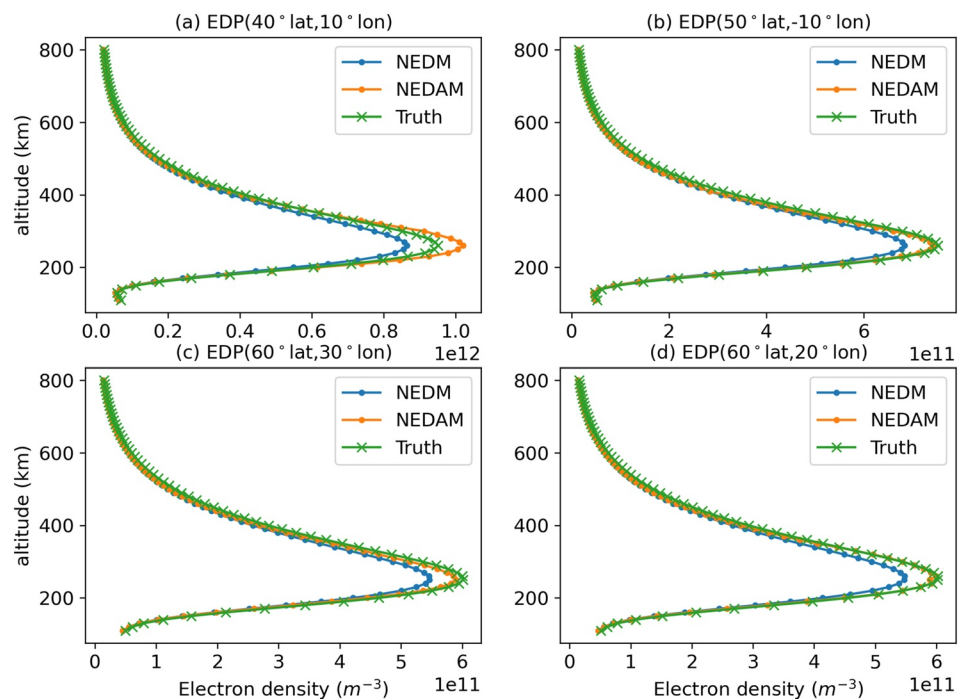
Figure 5. Comparisons among electron density profiles (EDPs) over selected grid points at 12:00 UT on day of year 61 in 2011. Location of the selected profiles is specified on each panel.
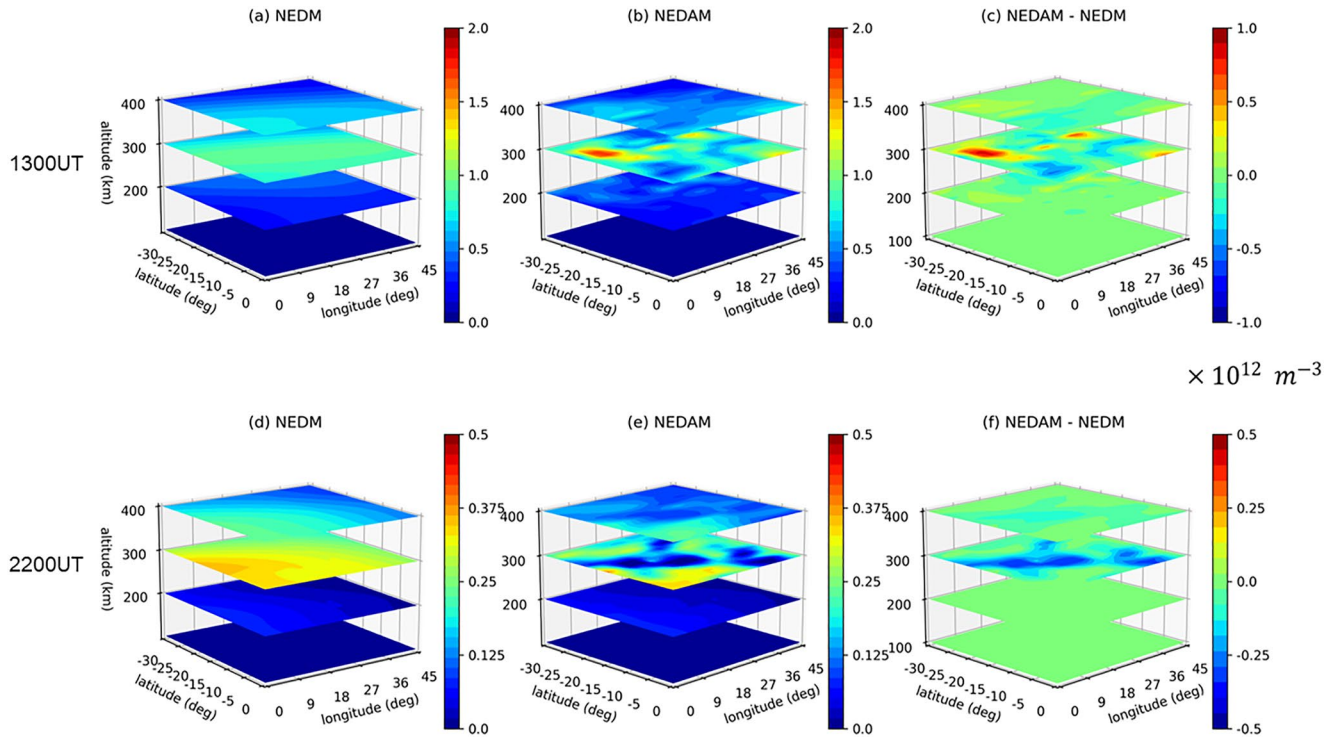
Figure 6. Horizontal slices of electron densities at 100, 200, 300, and 400 km altitude. (a, d) Background model (Neustrelitz Electron Density Model (NEDM)). (b, e) Data assimilation results using 4D-Var technique (Neustrelitz Electron Density Assimilation Model (NEDAM)). (c, f) Difference between NEDAM and NEDM. Electron density is given in units of 10^{12} m^{-3}.

is clearly seen. The lower peak is located at around 230 km and the upper peak at around 380 km. The dual peak structure seen in the NEDAM results is believed to be physically realistic. The local minimum at around 300 km (red lines in Figure 9b) is directly caused by the assimilated STEC because there is no extremum in the background model. In Figure 9b, there is a second peak at around 120 km for COSMIC profile, which is artificial by the spherical symmetry assumption in the Abel inversion. Generally speaking, the radio occultation technique is less reliable when the tangent height decreases because the profile is inverted from above. It is difficult to find another independent co-located measurement to verify the dual peak structure. However, the data assimilation can help in reducing the spatial gradient effect on the radio occultation inversion. Further studies on assimilation-based radio occultation inversion could provide some new insights in such large spatial gradient cases.

Moreover, the peak density in NEDAM is close to that in COSMIC profile, which is around 10^{11} m^{-3}. In both cases, the topside ionosphere electron density profile is well represented by NEDM. Drastic improvements in NEDAM of the improvements of two important parameters, that is, NmF2 and hmF2 are shown compared with the COSMIC radio occultation. In previous research the peak density height is not indicated or reconstructed well. It is difficult to well reconstruct the vertical structure of ionosphere by using only ground-based GNSS STEC observations (Bust et al., 2004; Lin et al., 2015; Ssessanga et al., 2019). There are two main reasons. The first reason can be that only few signals travel across some region above or below the hmF2 region and they are much larger than background electron density value so that the original maximum electron density in the corresponding column becomes lower than the updated electron density in the crossed region. In conclusion, if the distribution of observations is non-uniform or insufficient for current voxelization strategies, the hmF2 may be likely updated to a unreasonable value. However, it is likely to further improve the vertical structure by assimilating other observations like ionosondes or radio occultations. Second, the vertical correlation length might be highly variable and not uniquely determined. The scheme's ability to correctly estimate the peak height (hmF2) is seldomly analyzed because the commonly used assimilation data such as STEC have a minimal effect on hmF2 (Ssessanga et al., 2019). Although there are changes in hmF2 after assimilation, the accuracy of hmF2 is not discussed because assimilation of GNSS ground-based receiver STEC has already been found in other studies to have little or no effect on hmF2 variation (McNamara et al., 2011). However, the reason why the hmF2 is much less affected by the asssimilated STEC might be the 30-degree elevation
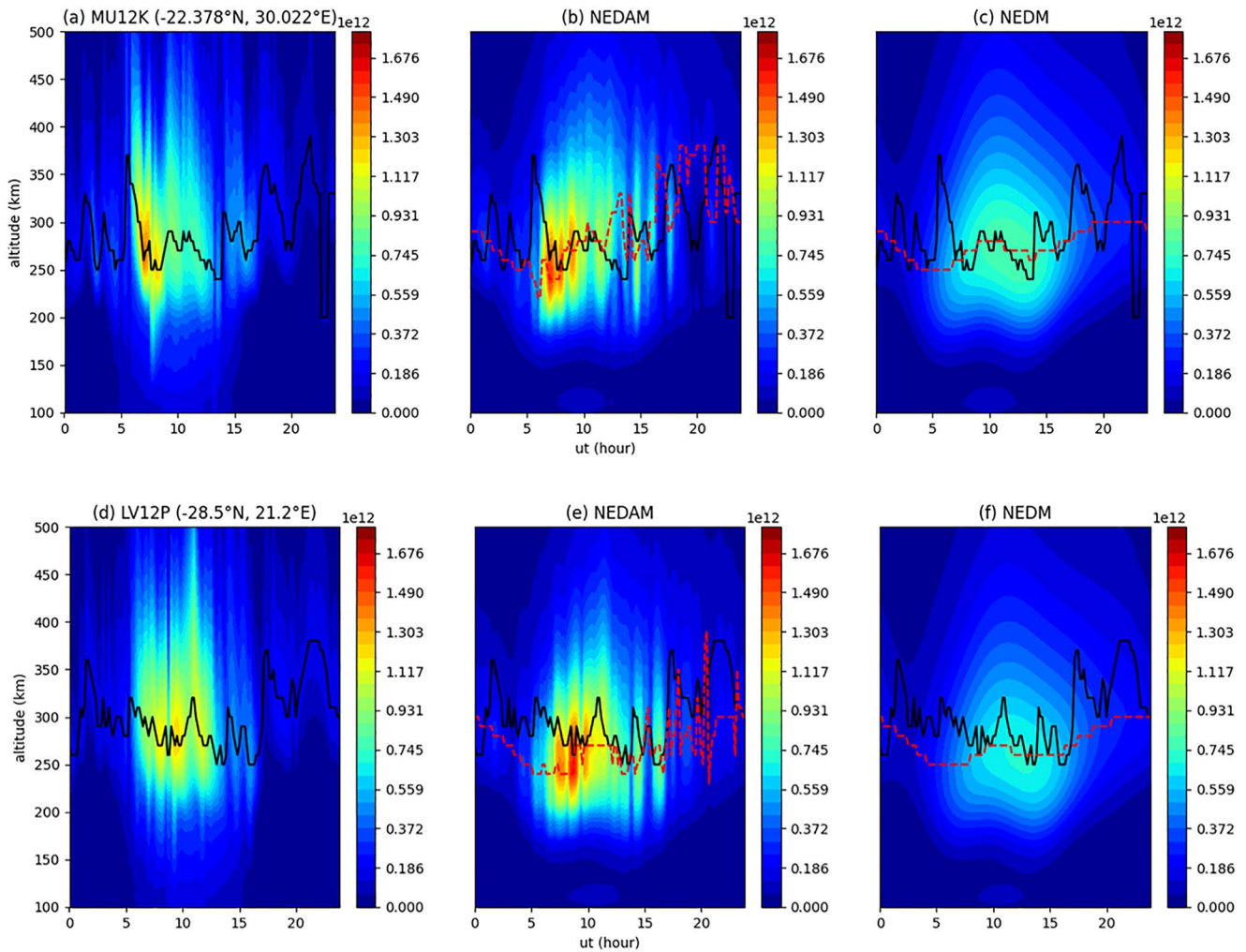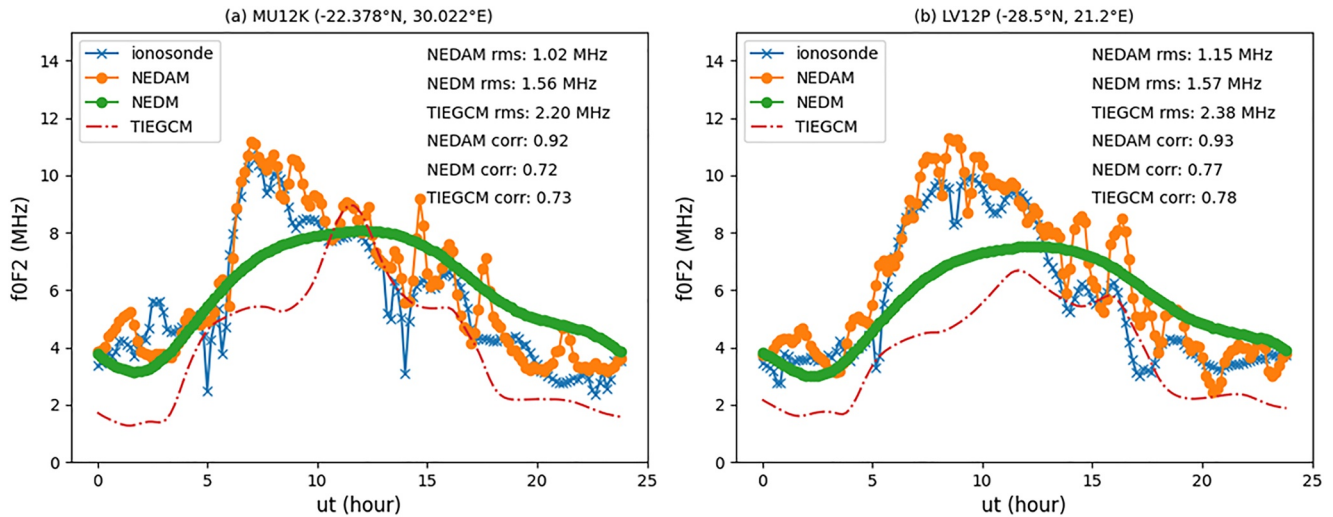
Figure 7. Comparison of electron densities between Neustrelitz Electron Density Assimilation Model (NEDAM), Neustrelitz Electron Density Model (NEDM), and ionosondes on 8 September 2017. Panels (a, d) show the ionosonde observations. Panel (b, e) show the NEDAM assimilation results. Panel (c, f) show the NEDM background electron densities. The black lines represent the ionosonde hmF2 and the red dashed line shows the model hmF2.

angle cutoff which is mentioned in Ssessanga et al. (2019). If one use only STECs with high elevation angles, the vertical structure is inevitably missing in the assimilations because those observations with high elevation angles can provide mainly the horizontal information rather than vertical structure. Generally speaking, the smaller the elevation angle is, the more information we can retrieve in the vertical direction. In addition to the large depletion of electron density above 300 km, we also found that in the second radio occultation profile the electron density value is negavtive through all altitudes below 260 km. In Figure 10, we plot the NEDAM electron density distribution at 260 km at 22:11 UT and the superimposed perigee trajectory at around 22:11 UT for C006 satellite. Note that the GNSS pierce point distributions can be found in Figure 1. It is evident that a large meridional gradient at 260 km was present along the radio occultation line-of-sight direction. This gradient gives rise to a break of local spherical symmetry and contaminate the final electron density profile especially below 300 km. Besides, it is intuitive to expect a better or more realistic electron density profile if we add radio occultation TEC into the assimilation directly. At the same time, the radio occultation STEC provides mostly the vertical electron density structure thanks to its low elevation angles. This is also one of the most interesting outlooks for NEDAM in the near future.

5. Conclusions

We have successfully developed NEDAM, a four-dimensional variational assimilation (4D-Var) scheme for ionospheric electron density reconstruction. We verify NEDAM using simulated data from a European GNSS ground

Figure 8. Comparison of critical frequency of F2 layer (foF2) among Neustrelitz Electron Density Assimilation Model, Neustrelitz Electron Density Model and ionosondes. Panel (a, b) show comparisons of foF2 at two ionosondes: MU12K and LV12P, respectively. The red dashed line shows the physics-based TIEGCM results.

network. In addition, the performance of NEDAM is validated using two ionosondes and radio occultation-derived electron density profiles from the COSMIC-1 mission during the September 2017 geomagnetic storm period. The main conclusions are as follows:

1. In the VTEC domain, provided that the ground-based GNSS networks are dense, it is shown that NEDAM captures well the horizontal structures of the ionospheric electron density using GNSS TEC simulations;
2. The critical frequency of the F2 layer in NEDAM is much more accurate than that of NEDM when compared with two ionosondes in the African region. During the storm period, the RMSE of the critical frequency of F2 is improved by 0.54 and 0.42 MHz at the stations MU12K and LV12P, respectively. We show that NEDAM also outperforms the physics-based TIEGCM driven by observed geophysical indices;
3. We compare the only two co-located electron density profiles from the COSMIC-1 with NEDAM and NEDM. NEDAM is found to reconstruct well not only the peak density but also the peak density height, which is lacking in previous studies.
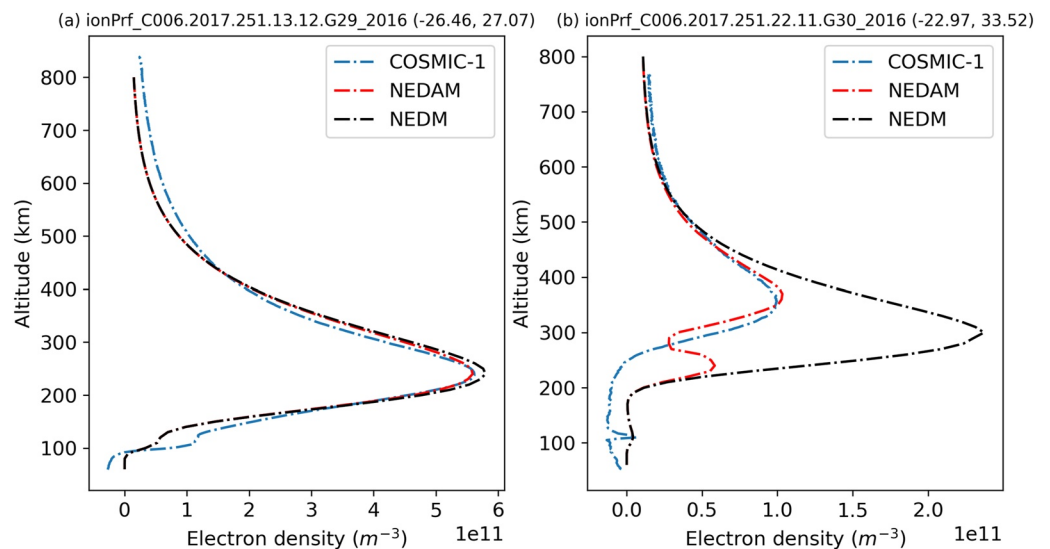
Figure 9. Comparison of electron density profiles among Neustrelitz Electron Density Assimilation Model, Neustrelitz Electron Density Model and COSMIC-1 radio occultation. Panel (a, b) shows the only two radio occultation events which are co-located on 8 September 2017. The numbers in brackets of titles represent the geographical latitude and longitude of perigee points.
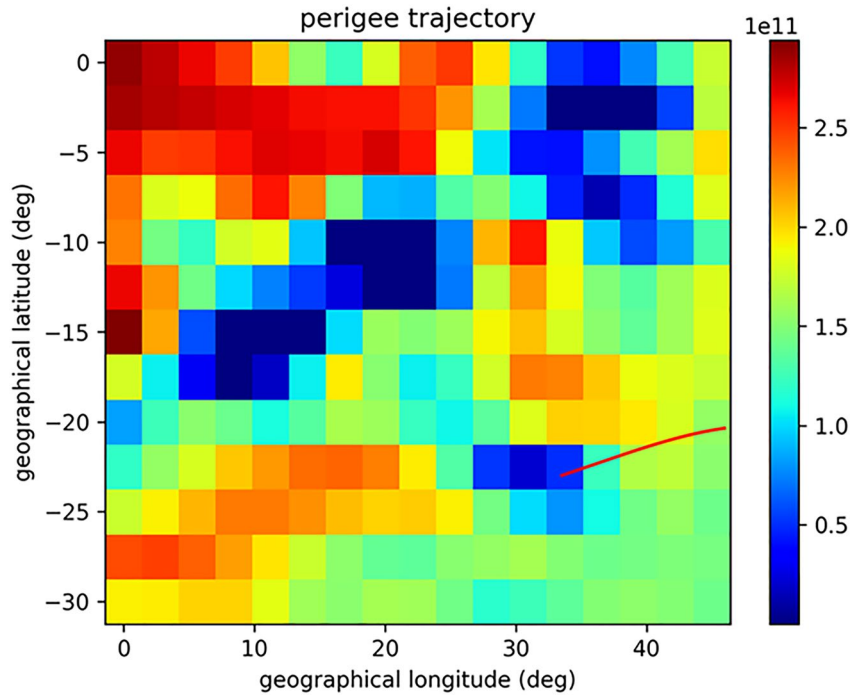
Figure 10. The colormap represents the Neustrelitz Electron Density Assimilation Model electron density at 260 km at 22:11 UT. Superimposed is the perigee trajectory of the radio occultation event at 22:11 UT for C006 satellite (Unit: el/m3).

All available and suitable real-time observations will be assimilated into NEDAM in the near future. And the post-processing version of NEDAM remains to be introduced with more kinds of observations of multiple latencies. In addition, the effect of including measurement geometry in the observation covariances should be studied in details.

As this is a preliminary study, there are still some issues to be addressed and some improvements to be made. One of the main problems to be solved is the lack of a comprehensive study of the background model error. This should be done by comparisons with measurements such as ionosonde or radio occultation measurements in the next generation of NEDAM. The second main problem is how to well define the correlation length, especially the vertical correlation length. A comprehensive study of the vertical correlation length for NEDM is required for the reconstruction of a better electron density profile and remains to be demonstrated in a future study. Finally, as an extension of the 4D-Var assimilation, a new 4D-Var version of NEDAM is also being developed in two directions: physics-based forward model and reduced dynamical model, for example, using the TIEGCM. The inclusion of the physics-based forecast model provides the opportunity to retrieve other quantities such as thermospheric neutral mass density responses due to ion convections in the upper atmosphere via a weakly constrained 4D-Var (Yuan & Jin, 2021).

Appendix A: Derivation of Equation (15a)

It is evident that $f(x_i, x_j) := Ne(x_i)Ne(x_j)$ is a Lebesgue-measurable function on $\mathbb{R}^2$ with $(x_i, x_j) \in \mathbb{R}^2$. Making use of Fubini's theorem and the linearity of mathematical expectations in the Lebesgue measure space $(R, \mathcal{F}, m) \times (R, \mathcal{F}, m)$, we may derive the covariance between two STEC observations as follows:

$$\mathrm{Cov}\big(\mathrm{STEC}_{s_i}, \mathrm{STEC}_{s_j}\big) = \mathrm{Cov}\left(\int_{s_i} Ne(x_i)\, dx_i + b_{s_i}, \int_{s_j} Ne(x_j)\, dx_j + b_{s_j} \right)$$

$$= E\left(\left(\int_{s_i} Ne(x_i) dx_i + b_{s_i} \right)\left(\int_{s_j} Ne(x_j)\, dx_j + b_{s_j} \right) \right) - E\left(\int_{s_i} Ne(x_i)\, dx_i + b_{s_i} \right) E\left(\int_{s_j} Ne(x_j)\, dx_j + b_{s_j} \right)$$

$$= E\left(\int_{s_i} \mathrm{Ne}(x_i)\, dx_i \int_{s_j} \mathrm{Ne}(x_j)\, dx_j\right) - E\left(\int_{s_i} \mathrm{Ne}(x_i)\, dx_i\right) E\left(\int_{s_j} \mathrm{Ne}(x_j)\, dx_j\right) + \mathrm{Cov}\left(b_{s_i}, b_{s_j}\right)$$

$$= E\left(\iint_{s_i s_j} \mathrm{Ne}(x_i)\mathrm{Ne}(x_j)\, dx_i dx_j\right) - E\left(\int_{s_i} \mathrm{Ne}(x_i)\, dx_i\right) E\left(\int_{s_j} \mathrm{Ne}(x_j)\, dx_j\right) + \mathrm{Cov}\left(b_{s_i}, b_{s_j}\right)$$

$$= \iint_{s_i s_j} \Big(E\left(\mathrm{Ne}(s_i)\mathrm{Ne}(s_j)\right) - E\left(\mathrm{Ne}(s_i)\right) E\left(\mathrm{Ne}(s_j)\right) \Big)\, dx_i dx_j + \mathrm{Cov}\left(b_{s_i}, b_{s_j}\right)$$

$$= \iint_{s_i s_j} \mathrm{Cov}\left(\mathrm{Ne}(s_i)\mathrm{Ne}(s_j)\right)\, dx_i dx_j + \mathrm{Cov}\left(b_{s_i}, b_{s_j}\right)$$

In practical applications, it is straightforward to rewrite the formula into a discrete form and integrate it numerically. Consider the Fourier transform of G_1,

$$\hat{G}_1(w) = \mathcal{F}(G_1(x)) = \int_{-\infty}^{+\infty} \exp\left(-\frac{1}{2}\left(\frac{x}{l}\right)^2\right)\exp(-iwx)\, dx$$

Since $G_1(x)$ is an even function, this integral is necessarily real and can be calculated as follows:

$$\int_{-\infty}^{+\infty} \exp\left(-\frac{1}{2}\left(\frac{x}{l}\right)^2\right)\exp(-iwx)\, dx = 2\sqrt{2}l \int_{0}^{+\infty} \exp\left(-x^2\right)\cos(lwx)\, dx = l\sqrt{2\pi}\exp\left(-\frac{(lw)^2}{4}\right) > 0 \quad \text{for all } l > 0$$

Hence the fact that the Gaussian correlation function $G(x_i, x_j)$ is indeed a legitimate correlation function may be guaranteed by the following lemma (Gaspari & Cohn, 1999).

If G_1 is an even function defined on $\mathbb{R}^n$, $G_1 \in L^1(\mathbb{R}^n)$ and $G_1(0) = 1$. The function $\mathrm{G}(x, y): R^n \times R^n \to \mathrm{R}$

$$\mathrm{G}(\mathrm{x}, \mathrm{y}) = G_1(\mathrm{x} - \mathrm{y})$$

is a homogeneous correlation function on $\mathbb{R}^n$ if and only if the Fourier transform $\hat{G}_1(w)$ of $G_1(x)$ is everywhere non-negative. And the three-dimensional function $\mathrm{G}(\vec{x}, \vec{y})$ which is the product of three one-dimensional Gaussian correlation functions is also a correlation function.

Data Availability Statement

The GIRO datasets were downloaded from https://www.ngdc.noaa.gov/stp/IONO/. The Madrigal database can be found at http://cedar.openmadrigal.org/list. The COSMIC-1 radio occultation data can be found at the CDAAC website https://cdaac-www.cosmic.ucar.edu/. The open-source TIE-GCM code is available at the website <http://www.hao.ucar.edu/modeling/tgcm>

References

Bust, G. S., Coker, C., Coco, D., Gaussiran, T. L., II., & Lauderdale, T. (2001). IRI data ingestion and ionospheric tomography. *Advances in Space Research*, *27*(1), 157–165. https://doi.org/10.1016/S0273-1177(00)00163-0

Bust, G. S., Garner, T. W., & Gaussiran, T. L., II. (2004). Ionospheric data assimilation three-dimensional (IDA3D): A global, multisensor, electron density specification algorithm. *Journal of Geophysical Research*, *109*(A11), A11312. https://doi.org/10.1029/2003JA010234

Bust, G. S., & Immel, T. J. (2020). IDA4D: Ionospheric data assimilation for the ICON mission. *Space Science Reviews*, *216*(3), 33. https://doi.org/10.1007/s11214-020-00648-z

Courtier, P., Thépaut, J.-N., & Hollingsworth, A. (1994). A strategy for operational implementation of 4D-Var, using an incremental approach. *Quarterly Journal of the Royal Meteorological Society*, *120*(519), 1367–1387. https://doi.org/10.1002/qj.49712051912

Gaspari, G., & Cohn, S. E. (1999). Construction of correlation functions in two and three dimensions. *Quarterly Journal of the Royal Meteorological Society*, *125*(554), 723–757. https://doi.org/10.1002/qj.49712555417

Hagan, M. E., Roble, R. G., & Hackney, J. (2001). Migrating thermospheric tides. *Journal of Geophysical Research*, *106*(A7), 12739–12752. https://doi.org/10.1029/2000JA000344

Heelis, R. A., Lowell, J. K., & Spiro, R. W. (1982). A model of the high-latitude ionospheric convection pattern. *Journal of Geophysical Research*, *87*(A8), 6339–6345. https://doi.org/10.1029/JA087iA08p06339

Hoque, M. M., & Jakowski, N. (2011). A new global empirical NmF2 model for operational use in radio systems. *Radio Science*, *46*(06), 1–13. https://doi.org/10.1029/2011RS004807

Hoque, M. M., & Jakowski, N. (2012). A new global model for the ionospheric F2 peak height for radio wave propagation. *Annales Geophysicae*, *30*(5), 797–809. https://doi.org/10.5194/angeo-30-797-2012

Hoque, M. M., Jakowski, N., & Prol, F. S. (2022). A new climatological electron density model for supporting space weather services. *Journal of Space Weather and Space Climate*, *12*, 1. https://doi.org/10.1051/swsc/2021044

Howe, B. M., Runciman, K., & Secan, J. A. (1998). Tomography of the ionosphere: Four-dimensional simulations. *Radio Science*, *33*(1), 109–128. Jan.-Feb. https://doi.org/10.1029/97RS02615

Jakowski, N., & Hoque, M. M. (2018). A new electron density model of the plasmasphere for operational applications and services. *Journal of Space Weather and Space Climate*, *8*, A16. https://doi.org/10.1051/swsc/2018002

Jakowski, N., Mayer, C., Hoque, M. M., & Wilken, V. (2011). Total electron content models and their use in ionosphere monitoring. *Radio Science*, *46*(6), RS0D18. https://doi.org/10.1029/2010RS004620

Kronschnabl, G., Coker, C., Gaussiran, T. L., II, Bust, G. S., & Coco, D. S. (1997). Using TRAITS to specify scintillation and propagation error over large regions. In *Paper presented at space weather effects on propagation of navigation and communication signals*. COMSAT Corp.

Lin, C. Y., Matsuo, T., Liu, J. Y., Lin, C. H., Tsai, H. F., & Araujo-Pradere, E. A. (2015). Ionospheric assimilation of radio occultation and ground-based GPS data using non-stationary background model error covariance. *Atmospheric Measurement Techniques*, *8*(1), 171–182. https://doi.org/10.5194/amt-8-171-2015

Lindgren, F., Rue, H., & Lindström, J. (2011). An explicit link between Gaussian fields and Gaussian Markov random fields: The stochastic partial differential equation approach. *Journal of the Royal Statistical Society: Series B*, *73*(4), 423–498. https://doi.org/10.1111/j.1467-9868.2011.00777.x

Manuel Hernández-Pajares□, M., Juan□, J. M., & Sanz□, J. (1999). New approaches in global ionospheric determination using ground GPS data. *Journal of Atmospheric and Solar-Terrestrial Physics*, *61*(16), 1237–1247. https://doi.org/10.1016/S1364-6826(99)00054-1

Manuel Hernández-Pajares□, M., Juan, J. M., Sanz, J., & Colombo, O. L. (2002). Improving the real-time ionospheric determination from GPS sites at very long distances over the equator. *Journal of Geophysical Research*, *107*(A10), 1296. https://doi.org/10.1029/2001JA009203

McNamara, L. F., Bishop, G. J., & Welsh, J. A. (2011). Assimilation of ionosonde profiles into a global ionospheric model. *Radio Science*, *46*(2), RS2006. https://doi.org/10.1029/2010RS004457

Norberg, J., Vierinen, J., Roininen, L., Orispaa, M., Kauristie, K., Rideout, W. C., et al. (2018). Gaussian Markov random field Priors in ionospheric 3-D multi-instrument tomography. *IEEE Transactions on Geoscience and Remote Sensing*, *56*(12), 7009–7021. https://doi.org/10.1109/TGRS

Prol, F. S., Kodikara, T., Hoque, M. M., & Borries, C. (2021). Global-scale ionospheric tomography during the March 17, 2015 geomagnetic storm. *Space Weather*, *19*(12), e2021SW002889. https://doi.org/10.1029/2021SW002889.2018.2847026

Qian, L., Solomon, S. C., & Kane, T. J. (2009). Seasonal variation of thermospheric density and composition. *Journal of Geophysical Research*, *114*(A1). https://doi.org/10.1029/2008JA013643

Raymund, T. D. (1995). Comparisons of several ionospheric tomography algorithms. *Annales Geophysicae*, *13*, 1254.

Raymund, T. D., Franke, S. J., & Yeh, K. C. (1994). Ionospheric tomography: Its limitations and reconstruction methods. *Journal of Atmospheric and Terrestrial Physics*, *56*(5), 637–657. https://doi.org/10.1016/0021-9169(94)90104-x

Richmond, A. D., Ridley, E. C., & Roble, R. G. (1992). A thermosphere/ionosphere general circulation model with coupled electrodynamics. *Geophysical Research Letters*, *19*(6), 601–604. https://doi.org/10.1029/92GL00401

Roininen, L., Lasanen, S., Orispää, M., & Särkkä, S. (2018). Sparse approximations of fractional Matérn fields. *Scandinavian Journal of Statistics*, *45*(1), 194–216. https://doi.org/10.1111/sjos.12297

Scherliess, L., Schunk, R. W., Sojka, J. J., & Thompson, D. C. (2004). Development of a physics-based reduced state Kalman filter for the ionosphere. *Radio Science*, *39*(1), RS1S04. https://doi.org/10.1029/2002RS002797

Schunk, R. W., Scherliess, L., Sojka, J. J., Thompson, D. C., Anderson, D. N., Codrescu, M., et al. (2004). Global assimilation of ionospheric measurements (GAIM). *Radio Science*, *39*(1), RS1S02. https://doi.org/10.1029/2002RS002794

Shim, J. S., Scherliess, L., Schunk, R. W., & Thompson, D. C. (2008). Spatial correlations of day-to-day ionospheric total electron content variability obtained from ground-based GPS. *Journal of Geophysical Research*, *113*(A9), A09309. https://doi.org/10.1029/2007JA012635

Ssessanga, N., Kim, Y. H., Choi, B., & Chung, J.-K. (2018). The 4D-var estimation of North Korean rocket exhaust emissions into the ionosphere. *Journal of Geophysical Research: Space Physics*, *123*, 2315–2326. https://doi.org/10.1002/2017JA024596

Ssessanga, N., Kim, Y. H., Habarulema, J. B., & Kwak, Y.-S. (2019). On imaging South African Regional Ionosphere using 4D-var technique. *Space Weather*, *17*(11), 1584–1604. https://doi.org/10.1029/2019SW002321

Yuan, L., Hoque, M., & Jin, S. (2021). A new method to estimate GPS satellite and receiver differential code biases using a network of LEO satellites. *GPS Solutions*, *25*(2), 71. https://doi.org/10.1007/s10291-021-01109-y

Yuan, L., Jin, S., & Hoque, M. (2020a). Estimation of GPS differential code biases based on independent reference station and recursive filter. *Remote Sensing*, *12*(6), 951. https://doi.org/10.3390/rs12060951

Yuan, L. L., & Jin, S. G. (2021). Observational evidence and formation mechanism of low-density cells in the upper thermosphere on 8 September 2017. *Journal of Geophysical Research: Space Physics*, *126*(2), e2020JA028915. https://doi.org/10.1029/2020JA028915

Yuan, L. L., Jin, S. G., & Hoque, M. (2020b). Estimation of LEO GPS receiver differential code bias based on inequality constrained least square and multi-layer mapping function. *GPS Solutions*, *24*(2), 57. https://doi.org/10.1007/s10291-020-0970-8

Yue, X., Wan, W., Liu, L., & Mao, T. (2007). Statistical analysis on spatial correlation of ionospheric day-to-day variability by using GPS and Incoherent Scatter Radar observations. *Annales Geophysicae*, *25*(8), 1815–1825. https://doi.org/10.5194/angeo-25-1815-2007